nature nanotechnology

ARTICLES

https://doi.org/10.1038/s41565-019-0607-7

Single-shot dynamics of spin–orbit torque and spin transfer torque switching in three-terminal magnetic tunnel junctions

Eva Grimaldi[1]*, Viola Krizakova[1], Giacomo Sala[1], Farrukh Yasin[2], Sébastien Couet[2], Gouri Sankar Kar[2], Kevin Garello[2]* and Pietro Gambardella[1]*

Current-induced spin-transfer torques (STT) and spin–orbit torques (SOT) enable the electrical switching of magnetic tunnel junctions (MTJs) in non-volatile magnetic random access memories. To develop faster memory devices, an improvement in the timescales that underlie the current-driven magnetization dynamics is required. Here we report all-electrical time-resolved measurements of magnetization reversal driven by SOT in a three-terminal MTJ device. Single-shot measurements of the MTJ resistance during current injection reveal that SOT switching involves a stochastic two-step process that consists of a domain nucleation time and propagation time, which have different genesis, timescales and statistical distributions compared to STT switching. We further show that the combination of SOT, STT and the voltage control of magnetic anisotropy leads to reproducible subnanosecond switching with the spread of the cumulative switching time smaller than 0.2 ns. Our measurements unravel the combined impact of SOT, STT and the voltage control of magnetic anisotropy in determining the switching speed and efficiency of MTJ devices.

Switching nanomagnets by current injection offers unparalleled scalability, as well as a low-power and high-speed operation compared to control via external magnetic fields[1–3]. Spin-transfer torques (STT)[1,4] are presently employed in memory and spin-logic applications[5,6] to control the state of magnetic tunnel junctions (MTJ) via an electric current that passes through the reference and free magnetic layers, which also allows for an efficient read-out of the MTJ through the tunnel magnetoresistance. Time-resolved studies of magnetization reversal in spin-valve[7,8] and MTJ devices[9–12] showed that STT enables switching on a timescale of 100 to 1 ns, depending on the driving current[13] and external field[14]. However, STT switching is characterized by non-reproducible dynamic paths and incubation times up to several tens of nanoseconds long, which limit the reliability and speed of the reversal process to about 10–20 ns, even when mitigation strategies based on large driving currents or non-collinear spin injection are employed[13,15,16].

These limitations may be overcome by magnetization reversal driven by spin–orbit torques (SOT)[3,17–19], as recently demonstrated in three-terminal MTJs with in-plane[20,21] as well as out-of-plane magnetization[22–25]. SOT switching combines an in-plane current injection geometry with charge-to-spin conversion due to the spin Hall effect and interfacial spin scattering[3]. Such a geometry decouples the write and read current paths, which improves the MTJ endurance and operation speed because it minimizes the electrical stress of the tunnel barrier and allows for the barrier thickness to be tuned for a high tunnel magnetoresistance, fast read-out and minimal read disturbances. Moreover, in devices with perpendicular magnetization, the injected spin current is orthogonal to the quiescent magnetization of the free layer, and thus provides an 'instant on' torque that is expected to minimize the switching incubation time[25–27].

Measurements of magnetic dots[27,28] and MTJs[23,29] performed after the injection of current pulses, as well as time-resolved stroboscopic measurements of magnetic dots performed using either pulsed X-ray[30] or laser probes[31,32], have succeeded in determining the probability and average speed of SOT-induced magnetization reversal. However, the stochastic nature of the transient dynamics as well as the actual speed of the individual switching events are not accessible in these experiments. Here we report real-time single-shot measurements of SOT switching in a three-terminal MTJ, which disclose the full reversal dynamics during the current injection, including both deterministic and stochastic events. Contrary to previous reports, we show that SOT switching involves a finite incubation time up to several nanoseconds long, which is determined by the interplay of current-induced SOT, in-plane field and Joule heating. By comparing the time-resolved magnetization reversal induced by SOT and STT in the same device, we evidence substantial differences in the dynamics, timescales and efficiency of the two mechanisms. Finally, by combining SOT, STT and voltage control of magnetic anisotropy (VCMA), we demonstrate subnanosecond switching with unprecedented reproducibility and a narrow distribution of the switching times.

Devices, measurement scheme and switching probability

Our samples consist of three-terminal perpendicularly magnetized MTJs with a top-pinned CoFeB reference layer, MgO tunnel barrier and a 0.9 nm-thick CoFeB free layer deposited on a 3.7 nm-thick β-phase W current line[25]. The MTJ pillars have a circular cross-section with a diameter of 80 nm (Fig. 1a,b). The orientation of the magnetization of the free layer, either up (+z) or down (−z), is detected through the changes of the tunnel magnetoresistance (R_{MTJ}), as shown in Fig. 1c for the minor loop recorded as a function of the out-of-plane external field (H_z). The loop shows a 100% remanence and sharp transitions between the parallel (P) and anti-parallel (AP) MTJ states, which indicates a full-reversal of the

[1]Department of Materials, ETH Zurich, Zürich, Switzerland. [2]imec, Leuven, Belgium. *e-mail: eva.grimaldi@mat.ethz.ch; Kevin.Garello@imec.be; pietro.gambardella@mat.ethz.ch

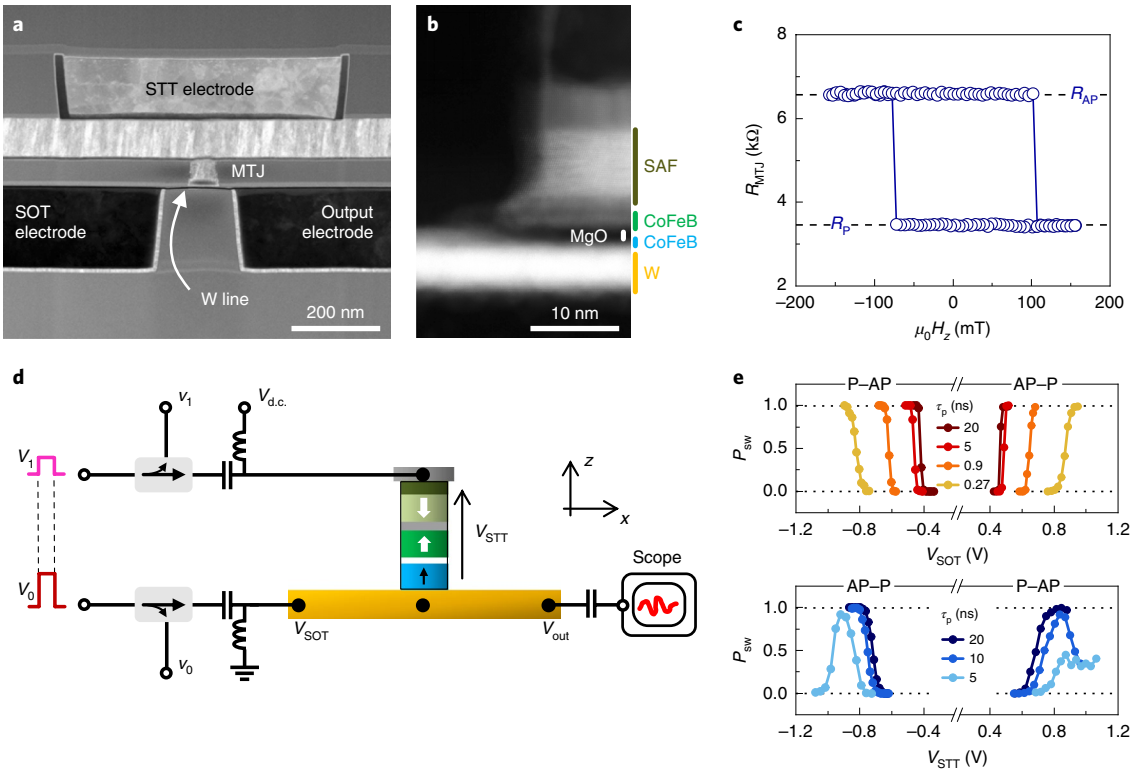

Fig. 1 | Schematic of the experimental set-up and three-terminal MTJ. a, Scanning electron microscope image of a three-terminal device with injection electrodes for SOT and STT switching. **b**, Detail of the MTJ pillar and W current line. SAF, synthetic antiferromagnet. **c**, Tunnelling magnetoresistance as a function of the external out-of-plane field. The 20 mT shift of the minor loop towards positive fields is due to the stray field of the top pinning layers, which favours the AP state. **d**, Electrical set-up for the time-resolved measurements of the tunnelling magnetoresistance during SOT and/or STT switching. **e**, Probability of SOT switching (top) at $\mu_0 H_x = -23$ mT and STT switching (bottom) at $\mu_0 H_x = 0$ mT as a function of the pulse amplitude for different pulse lengths. For each data point, P_{sw} is calculated over 200 set–reset events by measuring R_{MTJ} after each pulse.

magnetization with field. In the following, the magnetization of the reference layer points up, unless indicated otherwise.

Figure 1d shows a schematic of the three-terminal radiofrequency circuit used to bias the junction and the SOT current line, and to measure R_{MTJ} during switching. Two phase-matched radiofrequency pulses with a 0.15 ns rise time, variable length τ_p and amplitude V_0 and V_1 were injected into the feed lines of the bottom and top electrodes, biasing the MTJ at the driving voltages V_{SOT} and V_{STT} for SOT and STT switching, respectively. The resistance of the W line was $R_W = 309\,\Omega$ and those of the MTJ were $R_{MTJ} = 3.5\,k\Omega$ (P) and 6.5 kΩ (AP). As V_{SOT} itself generates a non-zero difference of electric potential between the top and bottom of the MTJ pillar, V_{STT} is a function of V_{SOT}, which in our case is given by $V_{STT} \approx 1.09(x - 0.46)V_{SOT}$, where $x = V_1/V_0$ (Methods and Extended Data Fig. 1). Thus, for SOT switching, we applied two pulses, V_0 and V_1, with the same polarity such that V_{STT} is either zero ($x = 0.46$) or very small ($x = 0.63$), with negligible effects on the magnetization dynamics (Methods and Extended Data Fig. 2). A non-zero V_{STT} is required for the time-resolved measurements to measure R_{MTJ} during the pulse injection. By varying x, we can study the entire bias range that spans from SOT to STT switching, and reveal effects due to the interplay of the two torques and VCMA. To study the magnetization dynamics during pulse injection, we measured the voltage at the output electrode of the MTJ using a 20 GHz real-time oscilloscope. The measured signal results from the sum of the currents that flow in-plane (V_{SOT}/R_W) and out-of-plane (V_{STT}/R_{MTJ}). The output voltage V_{sw}, normalized to the voltage difference before and after switching, corresponds to the variation of the out-of-plane magnetization of the free layer from the initial state ($V_{sw} = 0$) to the final state ($V_{sw} = 1$) (refs. [11–13,33], Methods and Extended Data Figs. 3 and 4).

The polarity of SOT switching is determined by the relative alignment of the current with the static in-plane magnetic field (H_x). This field is required to break the up–down degeneracy of the damping-like SOT and achieve a deterministic switching[3,17,30]. H_x is a free parameter in our study that can be eventually integrated in the MTJ design[34]. In our samples, $V_{SOT} > 0$ favours the up state and $V_{SOT} < 0$ favours the down state of the free layer for $H_x > 0$, and vice versa for $H_x < 0$, as expected for the negative spin Hall angle of β-W (ref. [35]). For STT switching, the polarity of V_{STT} sets the final state independently of H_x: $V_{STT} > 0$ favours the AP state, whereas $V_{STT} < 0$ favours the P state. When the SOT and STT were combined, we kept V_{STT} below the critical switching threshold and found that the final state was always the one promoted by SOT, which depends neither on the orientation of the reference layer nor on the sign of V_{STT}.

Figure 1e compares the after-pulse switching probability (P_{sw}) for the SOT and STT measured on the same device as a function of τ_p. The free layer has excellent switching properties under both an SOT and STT bias; however, the two switching mechanisms have very distinct characteristics. For SOT switching, P_{sw} is symmetric with respect to $\pm V_{SOT}$, whereas for STT switching P_{sw} is strongly asymmetric with respect to $\pm V_{STT}$. The decrease of P_{sw} at large $|V_{STT}|$ corresponds to conditions in which the switching is no longer deterministic and affected by back-hopping, which is stronger for AP–P transitions[11,12]. Moreover, SOT ensures a 100% switching for all values of τ_p down to 0.27 ns, whereas STT results in $P_{sw} < 1$ for $\tau_p < 10$ ns. The critical voltages (V_c) for SOT and STT switching, estimated at $P_{sw} = 0.5$, are about 0.4 and 0.75 V at

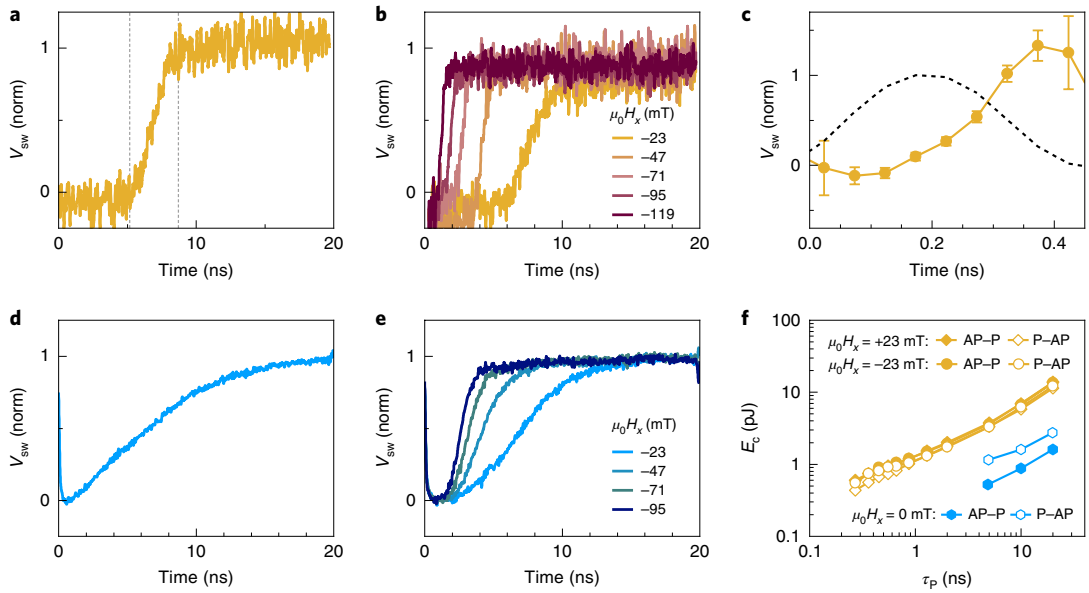

Fig. 2 | Average temporal evolution of the voltage signal during SOT and STT switching. a, V_{sw} (normalized) due to AP–P magnetization reversal induced by SOT at $\mu_0 H_x = +23$ mT, $V_{SOT} = +475$ mV and $\tau_p = 20$ ns averaged over 5,000 pulses. The dashed lines indicate the region in which the free-layer magnetization changed orientation during the multiple trials. **b**, Influence of H_x on the P–AP reversal induced by SOT with $V_{SOT} = +453$ mV (averaged over 5,000 pulses). **c**, Switching with subnanosecond current pulses: V_{sw} during the AP–P magnetization reversal at $\mu_0 H_x = +23$ mT and $V_{SOT} = +997$ mV averaged over 1,000 pulses with $\tau_p = 0.27$ ns and $V_{STT}/V_{SOT} = -0.5$. The data points are spaced by 50 ps, which corresponds to the sampling rate of our set-up. The dashed line shows the measured pulse shape. The error bars were calculated by adding in quadrature the noise of the switching and normalization voltage signals. **d**, V_{sw} due to the P–AP magnetization reversal induced by STT at $V_{STT} = +884$ mV, $\mu_0 H_x = 0$ mT and $\tau_p = 20$ ns averaged over 500 pulses. **e**, Influence of H_x on the P–AP reversal induced by STT with $V_{STT} = +756$ mV (averaged over 500 pulses). The time traces in **d** and **e** were offset prior to normalization to avoid division by close-to-zero values. In **a**, **b**, **d** and **e**, the pulses are 20 ns long and have the minimum amplitude required to achieve a 100% switching at the lowest field. **f**, Comparison of the critical switching energy for SOT (orange) and STT (blue) as a function of τ_p measured in the lowest field conditions ($|\mu_0 H_x| = 23$ mT for SOT and $\mu_0 H_x = 0$ mT for STT).

$\tau_p = 10$ ns, respectively. In the following, we focus on the switching dynamics at the minimum bias voltages required to achieve $P_{sw} = 1$ (measured up to 5,000 trials), unless indicated otherwise.

Time-resolved SOT and STT switching: average dynamics

We first report the time-resolved measurements of V_{sw} averaged over multiple SOT switching events. Figure 2a shows V_{sw} as a function of time, averaged over 5,000 pulses with $\tau_p = 20$ ns at a low field. A first striking observation is that, contrary to expectations[26,27,30–32], SOT switching occurs via a two-step process that involves a rather long incubation time of several nanoseconds, during which the free-layer magnetization appears to be at rest, and a shorter time during which the magnetization fully reverses from the initial to the final state. The incubation time decreases substantially on increasing either $|H_x|$ (Fig. 2b) or V_{SOT} (compare Fig. 2b,c), which makes it possible to achieve subnanosecond reversal with an extraordinarily narrow spread of the total switching time, comparable to the rising time of the current pulse (0.15 ns; Fig. 2c and Extended Data Fig. 5). These observations also show that the incubation time was probably too small to be detected in previous pump–probe experiments, which were carried out under relatively large currents and in-plane fields[30–32].

STT switching, performed on the same device, exhibits remarkably different dynamics and timescales compared to SOT. Figure 2d shows V_{sw} averaged over 500 pulses with $\tau_p = 20$ ns. In this average measurement, V_{sw} appears to change in a gradual way, evolving towards the final state over the entire duration of the pulse. This behaviour is in striking contrast with the SOT-induced reversal, for which V_{sw} remains quiescent and later increases within a few nanoseconds to full saturation, well before the pulse is completed. Increasing H_x lowers the total STT switching time, but not as strongly as for SOT (Fig. 2e). The two switching modes are thus characterized by distinct timescales, even though both STT[11–13,36,37] and SOT[30] switchings in perpendicular devices are known to occur via domain nucleation and propagation.

Our measurements also yield information on the critical energy $E_c(\tau_p) = V_c^2 \tau_p / R$ required to switch the free layer, where R is either R_W or R_{MTJ}. The large difference in the channel resistance for SOT and STT results in critical current densities of 2.0×10^8 A cm^{-2} for SOT and 2.3×10^6 A cm^{-2} (P–AP) or 4.2×10^6 A cm^{-2} (AP–P) for STT at $\tau_p = 10$ ns. Thus, even though V_c is lower, E_c is about an order of magnitude larger for SOT compared to STT for pulses longer than 5 ns. Reducing τ_p to 0.27 ns, however, leads to a minimum E_c of 0.4 pJ for SOT switching, which is unattainable by STT (Fig. 2f). These measurements show that SOT switching requires an improvement of the critical current density to become as efficient as STT at long timescales, but they also demonstrate that SOT allows for significant energy gains compared to STT because shorter pulses can achieve switching. A detailed discussion of the figures of merit relevant for SOT magnetic random access memory devices is reported in Supplementary Note 1.

Real-time dynamics of SOT and STT switching

To gain insight into the stochastic versus deterministic aspects of the switching process, we performed single-shot measurements at different biases and fields, which ranged from SOT- to STT-dominated switching. Figure 3a,b shows the time traces of V_{sw} measured during individual P–AP switching events at low and high in-plane fields for $V_{SOT} = +453$ mV (the minimum bias ensures $P_{sw} = 1$ in all cases). From left to right in Fig. 3a,b, these measurements show the evolution of SOT-driven switching with increasing contributions of the STT bias (from STT having a minor influence

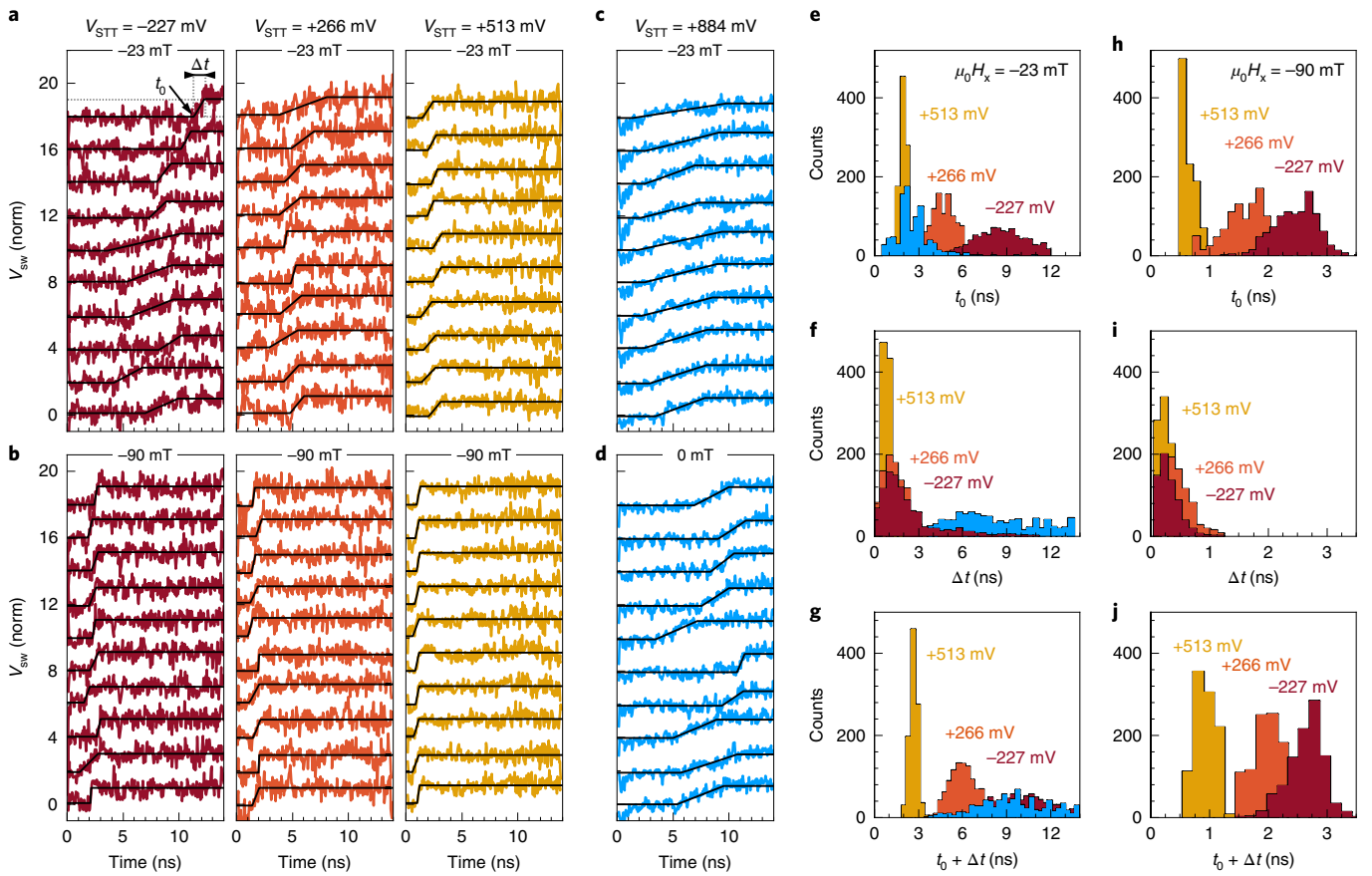

Fig. 3 | Single-shot measurements of SOT and STT switching. a,**b**, Representative voltage time traces recorded during ten individual SOT-induced P–AP switching events induced by 15 ns long pulses with $V_{SOT}=+453$ mV and an increasing STT bias $V_{STT}=-227$ mV (left), +266 mV (centre) and +513 mV (right) at $\mu_0 H_x=-23$ mT (**a**) and at $\mu_0 H_x=-90$ mT (**b**). **c**,**d**, Representative voltage time traces recorded during ten individual STT-induced P–AP switching events at $V_{STT}=+884$ mV for $\mu_0 H_x=-23$ mT (**c**) and $\mu_0 H_x=0$ mT (**d**). The time traces are vertically offset for clarity. Black solid lines are fits with a linear ramp used to extract t_0 and Δt. **e**–**g** Statistical distributions of the incubation time t_0 (**e**), transition time Δt (**f**) and the total switching time $t_0+\Delta t$ (**g**) for SOT switching at different STT biases (red, orange and yellow) and for STT switching (blue) with $\mu_0 H_x=-23$ mT. **h**–**j**, Statistical distributions of t_0 (**h**), Δt (**i**) and $t_0+\Delta t$ (**j**) with $\mu_0 H_x=-90$ mT. The histograms were obtained from the analysis of 1,000 single-shot switching events. AP–P switching measurements are reported in Extended Data Fig. 6.

against switching at $V_{STT}=-227$ mV to STT-assisted switching at $V_{STT}=+266$ and +513 mV).

All the time traces indicate deterministic switching from the initial to the final state before completion of the pulse, with no discernible intermediate states. However, for almost pure SOT at a low field, the magnetization reversal is characterized by significant trace-to-trace variations of the incubation and transition times. These variations, which are not discernible in pump–probe measurements[30–32], reveal the stochastic nature of the SOT reversal process. The ensuing fluctuations of the total switching time exceed by an order of magnitude predictions based on micromagnetic models in confined magnetic dots at finite temperature[38,39]. Importantly, very significant improvements in both the total time and the reproducibility of the reversal process were obtained by increasing either the STT bias or H_x, as shown in Fig. 3a,b. These improvements are all the more remarkable when compared with the time traces recorded for pure STT switching (Fig. 3c,d), which are characterized by slow transitions that last several nanoseconds.

Comparing the statistical distributions of the incubation and transition times measured as a function of bias and field yields further insight into the advantages of combining SOT with STT. We defined the incubation time t_0 and transition time Δt by fitting each time trace with a linear ramp that approximates the two-step switching process (solid lines in Fig. 3). Figure 3e–j report the distributions of t_0 and Δt determined from 1,000 identical single-shot measurements. Starting from almost pure SOT at a low field, which is characterized by broad incubation and transition time distributions with mean values $\bar{t}_0=9\pm2$ ns and $\overline{\Delta t}=2\pm2$ ns, respectively, we observed a strong reduction of $\bar{t}_0$ down to 2.0 ± 0.3 ns on increasing V_{STT} to +513 mV (Fig. 3e), accompanied by a narrowing of the transition times to $\overline{\Delta t}=0.8\pm0.3$ ns (Fig. 3f). Increasing H_x also has striking effects that lead to a drastic reduction of $\bar{t}_0$ to 0.7 ± 0.2 ns (Fig. 3h) and a more peaked distribution of $\overline{\Delta t}$ at around 0.4 ± 0.1 ns (Fig. 3i). In these conditions, we measured a total switching time $t_0+\Delta t$ with a mean of 0.9 ns and a s.d. of 0.16 ns (Fig. 3j). Incrementing the SOT bias also led to a significant reduction of the incubation time and distribution widths (Extended Data Fig. 7). Overall, we found that combining SOT with STT leads to s.d. values of $\bar{t}_0$ and $\overline{\Delta t}$ that are about an order of magnitude smaller compared to those of STT, even for strong overdrive conditions in non-collinear MTJs[15].

Origin of the incubation and transition times

The observation of a nanosecond-long incubation time contrasts with the fact that the SOT is orthogonal to the magnetization of the free layer, which leads to an 'instant-on' switching torque. Micromagnetic simulations, combined with finite element

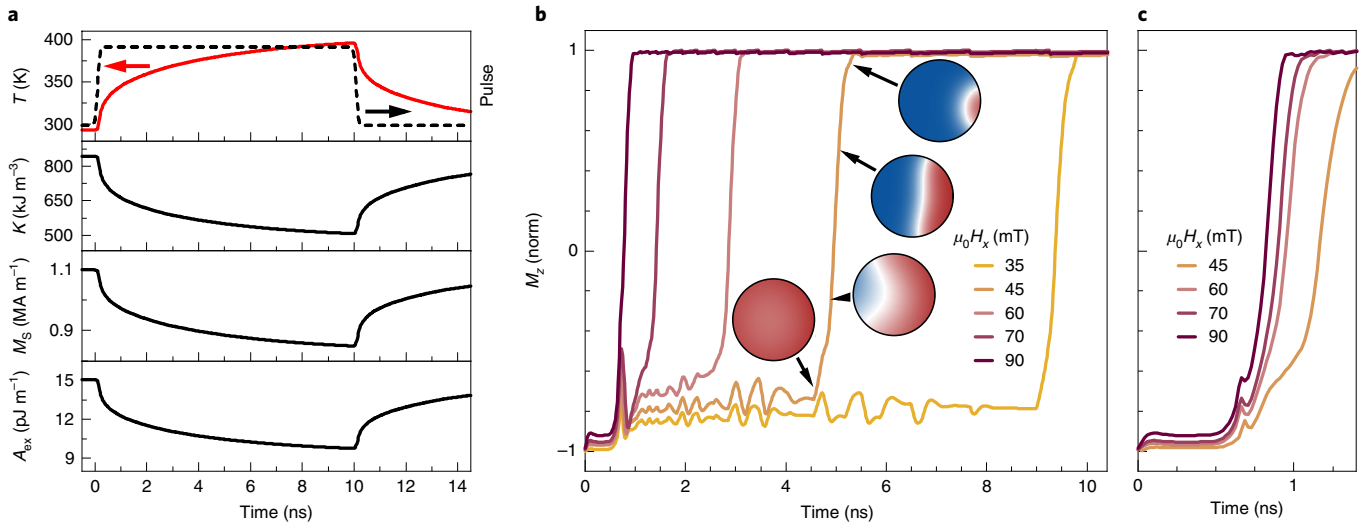

Fig. 4 | Temperature-induced variation of the magnetic parameters during pulse injection and micromagnetic simulations of SOT switching. a, From top to bottom: variation of temperature, magnetic anisotropy energy, saturation magnetization and exchange stiffness with time induced by a 10 ns current pulse (dashed line). **b**,**c**, Influence of H_x on the magnetization reversal for 10 ns (**b**) and 1 ns (**c**) pulses. The amplitude of the pulse is 1.10×10^8 A cm^{-2} in **a** and **b**, and 1.22×10^8 A cm^{-2} in **c**. The insets in **b** are snapshots of the magnetic configuration at different times during magnetization reversal at $\mu_0 H_x = 45$ mT.

simulations of current-induced heat dissipation in the MTJ (Methods), shed light on this apparent contradiction. First, the simulations confirm that SOT switching occurs in two steps, namely, the nucleation of a reverse domain at one edge of the free layer at the incubation time t_0 and the propagation of a domain wall towards the opposite edge during the transition time Δt. Second, the simulations reveal that the switching dynamics is strongly affected by the temporal evolution of the magnetic parameters of the free layer due to Joule heating (Fig. 4a). For V_{SOT} close to V_c, the SOT is not sufficient to initiate the reversal of a domain at the beginning of the pulse. The progressive increase of the temperature of the free layer during the current pulse induces a decrease of the magnetic anisotropy energy, which eventually lowers the energy barrier for domain nucleation and initiates the switching. Only the simulated time traces that include the temperature rise closely reproduce the experimental curves, which show a finite incubation time followed by a fast transition (Fig. 4b,c). The decrease of anisotropy has the strongest influence on t_0. Additional simulations show that the decrease of the saturation magnetization and exchange stiffness have minor effects. Further, we found that t_0 scales with H_x and V_{SOT}, in agreement with our measurements. The simulations thus demonstrate the origin of t_0 and Δt, which highlights the importance of thermal effects for the realistic modelling of SOT-induced switching.

Separation of VCMA and STT effects on SOT switching

The results shown in the previous sections highlight the strong gains in switching speed as well as reduced distribution widths that can be achieved by simultaneously biasing the SOT and STT electrodes of a three-terminal MTJ. Yet, if the reversal is dominated by the SOT, what is really the effect of V_{STT}? The STT bias is known to induce two different effects, namely STT[1,4] and a decrease or increase of the magnetic anisotropy of the free layer via the VCMA[40,41]. Both STT[24,42] and VCMA[43,44] have been shown to assist SOT switching in three-terminal MTJs; however, their separate influence as well as their effect on the magnetization dynamics have not been studied so far.

Here we distinguish the two effects by noting that the STT depends on the orientation of the magnetization of the reference layer, whereas the VCMA does not. Therefore, by inverting the reference layer using an external field, we can investigate the MTJ configurations in which the STT alternatively favours or hinders switching for a given polarity of the VCMA. Figure 5a,b illustrates the case of $V_{STT} > 0$ for the two opposite orientations of the reference layer; the possible combinations of SOT, STT and VCMA and their effects on switching are reported in Table 1. We first consider P–AP reversal for the reference layer pointing up, such that STT is expected to assist (oppose) switching for $V_{STT} > 0$ (<0). Figure 5c compares the averaged time traces obtained for negative and positive values of V_{STT} at constant V_{SOT}. Clearly, $V_{STT} > 0$ accelerates the reversal relative to $V_{STT} = 0$, whereas $V_{STT} < 0$, apart from reducing the noise level due to the increased bias of the junction, has only a minor effect on the dynamics. This bias asymmetry is also manifested in the critical SOT voltage V_c determined from the measurements of P_{sw} as a function of τ_p (Fig. 5d), which show that V_c reduces by up to 30% for $V_{STT} > 0$, whereas it does not change noticeably for $V_{STT} < 0$. This asymmetry is a first indication that STT is not the sole effect to influence the SOT-driven magnetization reversal.

To separate the effects of STT and VCMA, we plot in Fig. 5e the normalized critical voltages $\nu_c = V_c(V_{STT})/V_c(V_{STT}=0)$ that correspond to the reference layer magnetization pointing up ($\nu_c^{\uparrow}$) and down ($\nu_c^{\downarrow}$) for different values of V_{STT}. For the shorter τ_p, the main effect is a downward shift of both $\nu_c^{\uparrow}$ and $\nu_c^{\downarrow}$ for positive increments of V_{STT}, which is quantified by the average $\bar{\nu}_c = (\nu_c^{\uparrow} + \nu_c^{\downarrow})/2$ (Fig. 5f). For the longer τ_p, in addition to the shift of $\bar{\nu}_c$, we observed that $\nu_c^{\uparrow}$ became increasingly smaller than $\nu_c^{\downarrow}$, as reflected by the difference $\Delta\nu_c = (\nu_c^{\uparrow} - \nu_c^{\downarrow})/2$ (Fig. 5g). As $\bar{\nu}_c$ and $\Delta\nu_c$ are, respectively, even and odd with respect to the inversion of the reference layer, we ascribe the first effect to the VCMA and the second to STT.

The shift of $\bar{\nu}_c$ is consistent with a reduction of the magnetic anisotropy induced by a positive bias of the free layer. By assuming that the perpendicular magnetic anisotropy of the free layer scales proportionally to $\bar{\nu}_c$, we estimate a VCMA coefficient of 57 fJ V^{-1} m^{-1} for positive V_{STT} (Supplementary Note 2), which is in agreement with previous measurements of the VCMA in CoFeB/MgO (refs. [44,45]). However, $\Delta\nu_c$ is consistent with a scenario in which the STT adds or subtracts to the SOT depending on the relative sign of V_{STT} and reference layer magnetization (Table 1). $\Delta\nu_c$ increases with V_{STT} and τ_p, which thus shows that STT-assisted switching becomes relevant at larger bias and longer timescales. A likely scenario is that the SOT initiates the switching, mainly assisted by VCMA in lowering the

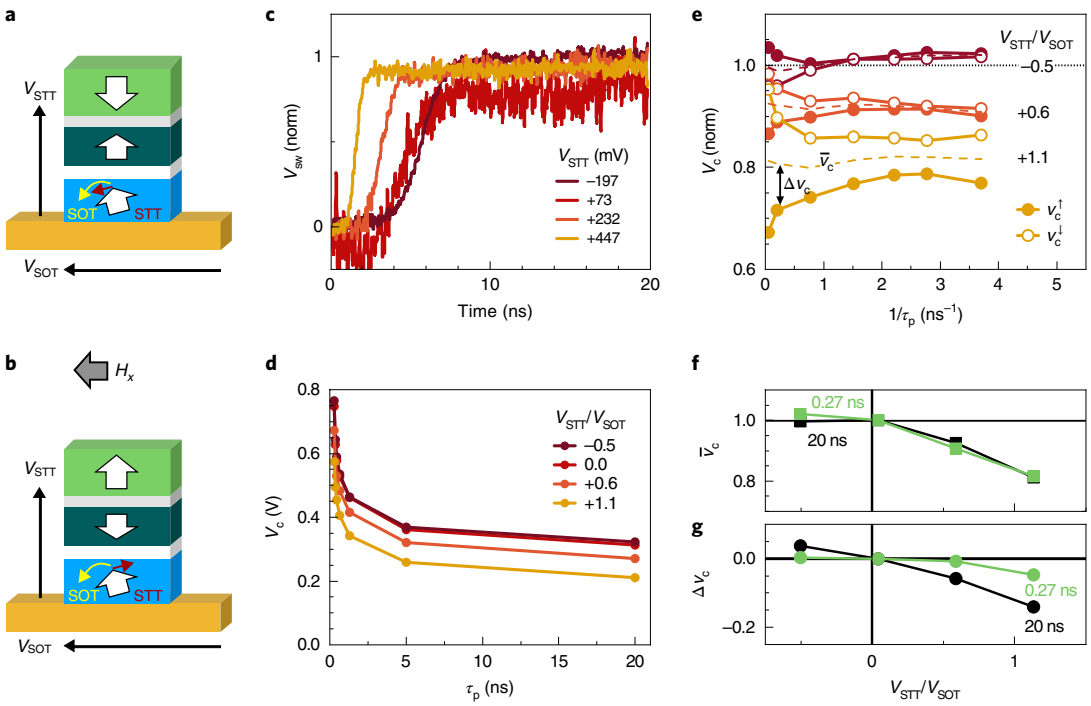

Fig. 5 | Combined effect of VCMA and STT on SOT-induced switching. a,**b**, Schematics of SOT-induced switching for the reference layer pointing up (**a**) and down (**b**). The black arrows indicate the bias and the white block arrows indicate the magnetization state. The yellow and red arrows schematize the switching directions favoured by SOT and STT, respectively. In **a**, STT assists the SOT-induced switching, whereas in **b**, STT opposes the switching. **c**, Averaged voltage time traces of SOT-induced P–AP switching with different STT biases, $V_{STT}=-197$, +73, +232 and +447 mV for $V_{SOT}=+394$ mV, and $\tau_p=20$ ns. **d**, Evolution of the critical voltage as a function of pulse length for different V_{STT}/V_{SOT} ratios. **e**, Normalized critical voltages $v_c^{\uparrow}$ and $v_c^{\downarrow}$ as a function of the inverse pulse length for different V_{STT}/V_{SOT} ratios. The magnetization of the reference layer points either up ($v_c^{\uparrow}$) or down ($v_c^{\downarrow}$) and correspond to the situations depicted in **a** and **b**, respectively. The data are shown as a function of $1/\tau_p$ to better evidence the timescales at which STT and VCMA are relevant. **f**,**g**, Evolution of the average critical voltage $\bar{v}_c$ (VCMA-like contribution) (**f**) and voltage asymmetry Δv_c (STT-like contribution) (**g**) as a function of V_{STT}/V_{SOT} for short and long pulses. All the measurements were performed at $\mu_0 H_x=-90$ mT and $V_{SOT}>0$, and correspond to P–AP (AP–P) switching for the reference layer magnetization pointing up (down) and free layer initially pointing up. Measurements performed for the free layer initially pointing down are reported in Extended Data Fig. 8.

Table 1 | Switching of a three-terminal MTJ

Reference layer	SOT switching		STT switching		SOT and STT	Δv_c	SOT and VCMA	$\bar{v}_c$
Up	$V_{SOT}>0$, $H_x<0$	P–AP	$V_{STT}>0$	P–AP	Add	<0	Add	<1
			$V_{STT}<0$	AP–P	Subtract	>0	Subtract	~1
Down	$V_{SOT}>0$, $H_x<0$	AP–P	$V_{STT}>0$	P–AP	Subtract	>0	Add	<1
			$V_{STT}<0$	AP–P	Add	<0	Subtract	~1

Magnetic configurations of the MTJ for up-to-down switching of the free layer induced by SOT and STT. The combined effects of STT and VCMA on SOT-induced switching are also shown, together with the observed changes of the normalized critical voltage asymmetry Δv_c and the average normalized critical voltage $\bar{v}_c$, respectively, relative to pure SOT switching. The entries in the table refer to $V_{SOT}>0$, $H_x<0$ and correspond to the data reported in Fig. 5. A complete list of all the possible combinations of SOT, STT and VCMA is given in Supplementary Note 3.

domain nucleation barrier, as suggested by the strong reduction of $\bar{t}_0$ (Fig. 3e,h), and then drives the propagation of a domain wall across the free layer assisted by STT, which modifies the damping of the free layer and, consequently, the domain wall speed (Fig. 3f,i).

Conclusions

Our results provide direct insight into the real-time dynamics of SOT-induced magnetization reversal, either alone or in combination with STT and VCMA. Close to the critical voltage, the SOT switching rate is limited by the time required to nucleate a reverse domain, which is strongly affected by Joule heating, whereas the transition time that corresponds to domain expansion is comparatively short. By taking advantage of the multiple bias and magnetic configurations of a three-terminal MTJ, we demonstrate different strategies to achieve a faster switching with an unprecedented uniformity and a narrow distribution of the individual switching events. The combination of SOT, VCMA and STT is particularly promising for reducing the latency and jitter of the writing process in logic and memory applications that require a high speed and non-volatility.

Online content

Any methods, additional references, Nature Research reporting summaries, source data, extended data, supplementary information, acknowledgements, peer review information; details of author contributions and competing interests; and statements of data and

code availability are available at https://doi.org/10.1038/s41565-019-0607-7.

Received: 27 May 2019; Accepted: 2 December 2019;
Published online: 27 January 2020

References

1. Brataas, A., Kent, A. D. & Ohno, H. Current-induced torques in magnetic materials. *Nat. Mater.* **11**, 372–381 (2012).
2. Kent, A. D. & Worledge, D. C. A new spin on magnetic memories. *Nat. Nanotechnol.* **10**, 187–191 (2015).
3. Manchon, A. et al. Current-induced spin–orbit torques in ferromagnetic and antiferromagnetic systems. *Rev. Mod. Phys.* **91**, 035004 (2019).
4. Ralph, D. C. & Stiles, M. D. Spin transfer torques. *J. Magn. Magn. Mater.* **320**, 1190–1216 (2008).
5. Apalkov, D., Dieny, B. & Slaughter, J. M. Magnetoresistive random access memory. *IEEE Proc.* **104**, 1796–1830 (2016).
6. Hanyu, T. et al. Standby-power-free integrated circuits using MTJ-based VLSI computing. *IEEE Proc.* **104**, 1844–1863 (2016).
7. Krivorotov, I. N. et al. Time-domain measurements of nanomagnet dynamics driven by spin-transfer torques. *Science* **307**, 228–231 (2005).
8. Liu, H. et al. Dynamics of spin torque switching in all-perpendicular spin valve nanopillars. *J. Magn. Magn. Mater.* **358–359**, 233–258 (2014).
9. Devolder, T. et al. Single-shot time-resolved measurements of nanosecond-scale spin-transfer induced switching: stochastic versus deterministic aspects. *Phys. Rev. Lett.* **100**, 057206 (2008).
10. Cui, Y. T. et al. Single-shot time-domain studies of spin-torque-driven switching in magnetic tunnel junctions. *Phys. Rev. Lett.* **104**, 097201 (2010).
11. Devolder, T. et al. Time-resolved spin-torque switching in MgO-based perpendicularly magnetized tunnel junctions. *Phys. Rev. B* **93**, 024420 (2016).
12. Devolder, T., Le Goff, A. & Nikitin, V. Size dependence of nanosecond-scale spin-torque switching in perpendicularly magnetized tunnel junctions. *Phys. Rev. B* **93**, 224432 (2016).
13. Hahn, C. et al. Time-resolved studies of the spin-transfer reversal mechanism in perpendicularly magnetized magnetic tunnel junctions. *Phys. Rev. B* **94**, 214432 (2016).
14. Tomita, H. et al. Single-shot measurements of spin-transfer switching in CoFeB/MgO/CoFeB magnetic tunnel junctions. *Appl. Phys. Express* **1**, 061303 (2008).
15. Bultynck, O. et al. Instant-on spin torque in noncollinear magnetic tunnel junctions. *Phys. Rev. Appl.* **10**, 054028 (2018).
16. Heindl, R., Rippard, W. H., Russek, S. E. & Kos, A. B. Physical limitations to efficient high-speed spin-torque switching in magnetic tunnel junctions. *Phys. Rev. B* **83**, 054430 (2011).
17. Miron, I. M. et al. Perpendicular switching of a single ferromagnetic layer induced by in-plane current injection. *Nature* **476**, 189–193 (2011).
18. Garello, K. et al. Symmetry and magnitude of spin–orbit torques in ferromagnetic heterostructures. *Nat. Nanotechnol.* **8**, 587–593 (2013).
19. Lee, S.-W. & Lee, K.-J. Emerging three-terminal magnetic memory devices. *IEEE Proc.* **104**, 1831–1843 (2016).
20. Liu, L. et al. Spin-torque switching with the giant spin Hall effect of tantalum. *Science* **336**, 555–558 (2012).
21. Fukami, S., Anekawa, T., Zhang, C. & Ohno, H. A spin–orbit torque switching scheme with collinear magnetic easy axis and current configuration. *Nat. Nanotechnol.* **11**, 621–625 (2016).
22. Cubukcu, M. et al. Spin–orbit torque magnetization switching of a three-terminal perpendicular magnetic tunnel junction. *Appl. Phys. Lett.* **104**, 042406 (2014).
23. Cubukcu, M. et al. Ultra-fast perpendicular spin–orbit torque MRAM. *IEEE Trans. Magn.* **54**, 1–4 (2018).
24. Wang, M. et al. Field-free switching of a perpendicular magnetic tunnel junction through the interplay of spin–orbit and spin-transfer torques. *Nat. Electron.* **1**, 582–588 (2018).
25. Garello, K. et al. SOT-MRAM 300MM integration for low power and ultrafast embedded memories. *IEEE Symposium on VLSI Circuits* https://ieeexplore.ieee.org/document/8502269 (2018).
26. Lee, K.-S., Lee, S.-W., Min, B.-C. & Lee, K.-J. Threshold current for switching of a perpendicular magnetic layer induced by spin Hall effect. *Appl. Phys. Lett.* **102**, 112410 (2013).
27. Garello, K. et al. Ultrafast magnetization switching by spin–orbit torques. *Appl. Phys. Lett.* **105**, 212402 (2014).
28. Zhang, C., Fukami, S., Sato, H., Matsukura, F. & Ohno, H. Spin–orbit torque induced magnetization switching in nano-scale Ta/CoFeB/MgO. *Appl. Phys. Lett.* **107**, 012401 (2015).
29. Aradhya, S. V., Rowlands, G. E., Oh, J., Ralph, D. C. & Buhrman, R. A. Nanosecond-timescale low energy switching of in-plane magnetic tunnel junctions through dynamic Oersted-field-assisted spin Hall effect. *Nano Lett.* **16**, 5987–5992 (2016).
30. Baumgartner, M. et al. Spatially and time-resolved magnetization dynamics driven by spin–orbit torques. *Nat. Nanotechnol.* **12**, 980–986 (2017).
31. Decker, M. M. et al. Time resolved measurements of the switching trajectory of Pt/Co elements induced by spin–orbit torques. *Phys. Rev. Lett.* **118**, 257201 (2017).
32. Yoon, J. et al. Anomalous spin–orbit torque switching due to field-like torque-assisted domain wall reflection. *Sci. Adv.* **3**, 1603099 (2017).
33. Sampaio, J. et al. Time-resolved observation of fast domain-walls driven by vertical spin currents in short tracks. *Appl. Phys. Lett.* **103**, 242415 (2013).
34. Garello, K. et al. Manufacturable 300 mm platform solution for field-free switching SOT-MRAM. *IEEE Symposium on VLSI Technology* https://doi.org/10.23919/VLSIT.2019.8776537 (2019).
35. Pai, C.-F. et al. Spin transfer torque devices utilizing the giant spin Hall effect of tungsten. *Appl. Phys. Lett.* **101**, 122404 (2012).
36. Sun, J. Z. et al. Effect of subvolume excitation and spin-torque efficiency on magnetic switching. *Phys. Rev. B* **84**, 064413 (2011).
37. Chaves-O'Flynn, G. D., Wolf, G., Sun, J. Z. & Kent, A. D. Thermal stability of magnetic states in circular thin-film nanomagnets with large perpendicular magnetic anisotropy. *Phys. Rev. Appl.* **4**, 024010 (2015).
38. Martinez, E. et al. Universal chiral-triggered magnetization switching in confined nanodots. *Sci. Rep.* **5**, 10156 (2015).
39. Mikuszeit, N. et al. Spin–orbit torque driven chiral magnetization reversal in ultrathin nanostructures. *Phys. Rev. B* **92**, 144424 (2015).
40. Weisheit, M. et al. Electric field-induced modification of magnetism in thin-film ferromagnets. *Science* **315**, 349–351 (2007).
41. Maruyama, T. et al. Large voltage-induced magnetic anisotropy change in a few atomic layers of iron. *Nat. Nanotechnol.* **4**, 158–161 (2009).
42. Wang, Z., Zhao, W., Deng, E., Klein, J.-O. & Chappert, C. Perpendicular-anisotropy magnetic tunnel junction switched by spin-Hall-assisted spin-transfer torque. *J. Phys. D* **48**, 065001 (2015).
43. Kato, Y. et al. Improvement of write efficiency in voltage-controlled spintronic memory by development of a Ta–B spin Hall electrode. *Phys. Rev. Appl.* **10**, 044011 (2018).
44. Yoda, H. et al. High-speed voltage-control spintronics memory (high-speed VoCSM). *IEEE International Memory Workshop* https://doi.org/10.1109/IMW.2017.7939085 (2017).
45. Zhu, J. et al. Voltage-induced ferromagnetic resonance in magnetic tunnel junctions. *Phys. Rev. Lett.* **108**, 197203 (2012).

Methods

Sample fabrication. The three-terminal MTJ devices were fabricated on imec's 300 mm MRAM pilot line[33]. First, damascene W bottom electrode contacts (for the SOT and output electrodes) were patterned on a plasma-enhanced chemical vapour deposition SiO_2 substrate and planarized. The stack shown in Fig. 1a,b was then deposited in situ at room temperature by physical vapour deposition in a 300 mm cluster tool (EC7800 Canon-Anelva). After deposition, the stack was annealed at 300 °C for 30 min in a magnetic field of 1 T. The MTJ consists of a perpendicularly magnetized top-pinned stack of composition (nm) W(3.7)/$Co_{20}Fe_{60}B_{20}$(0.9)/MgO(~1)/$Co_{17.5}Fe_{52.5}B_{30}$(1.1)/W(0.3)/synthetic antiferromagnet(10.5). The resistance area product of the MgO layer was RA = 14 Ω μm². The bottom layer was made of β-phase W with a resistivity of 140 μΩ cm and an effective spin Hall angle of −0.32 (ref. [25]); the combined resistivity of the W/$Co_{20}Fe_{60}B_{20}$ bilayer was 120 μΩ cm. The $Co_{17.5}Fe_{52.5}B_{30}$ reference layer was ferromagnetically coupled through a W spacer to a perpendicular synthetic antiferromagnet that consisted of Co(1.2)/Ru(0.85)/Co(0.6)/Pt(0.8)/[Co(0.3)/Pt(0.8)]$_6$. The perpendicular anisotropy field and thermal stability factor of the free layer, $H_K = 270$ mT and $\Delta = 50\,k_BT$, respectively, were estimated by measuring the switching probability as a function of external field H, $P_{sw}(H)$, applied parallel to the easy axis, and fitting it by:

$$P_{sw}(H) = 1 - \exp\left[\frac{-H_K f_0 \sqrt{\pi}}{2r\sqrt{\Delta}} \mathrm{erfc}\left[\sqrt{\Delta}\left(1 - \frac{H}{H_K}\right)\right]\right] \quad (1)$$

where r is the field sweep rate and f_0 the attempt frequency (here set to 1 GHz) (ref. [46]).

The MTJ pillar was defined using 193 nm immersion lithography and ion-beam etching at normal and grazing angles with specific stop conditions based on end-point detection to leave the W layer intact while patterning the pillar without producing sidewall shorts across the MgO barrier. The W layer was then patterned by lithography and ion-beam etched to form a 220 nm-wide current line with resistance $R_W = 309\,\Omega$. Finally, a dual damascene Cu top electrode (STT electrode) was fabricated to complete the electrical connection (Fig. 1a).

Electrical set-up. The electrical set-up consisted of radiofrequency and d.c. paths, which were decoupled by bias tees and a d.c. block, as shown in Fig. 1d. The d.c. path was used for after-pulse measurements of R_{MTJ}. The radiofrequency path is used to inject the radiofrequency pulses for current-induced switching and time-resolved measurements. Pulses of length $\tau_p = 0.27$–20 ns, defined as the full-width at half-maximum of the injected pulse, are generated by a single pulse generator with a 0.15 ns rise time. Each pulse was split by a power divider into two identical pulses that were then independently attenuated to adjust the ratio $x = V_1/V_0$ between the pulses applied to the STT and SOT feed lines. In the case of STT switching, the SOT terminal was disconnected from the output of the power divider and both ends connected to ground through a 50 Ω resistance. A 20 dB directional coupler was placed on each injection line to dissipate the back-reflected pulses, and the coupled ports v_0 and v_1 were connected to the oscilloscope and used to trigger and calibrate the switching pulse amplitudes. The time-resolved signal V_{out} was acquired on a third input of the oscilloscope. According to our coordinate system, $V_{SOT} > 0$ generates a current flowing along $+x$ and $V_{STT} > 0$ a current flowing along $-z$.

Equivalent resistance model of a three-terminal MTJ. The equivalent resistance of a three-terminal device is presented in Extended Data Fig. 1. The STT bias is given by $V_{STT} = v_t - v_b$, where v_t and v_b are the voltages applied to the top and bottom of the MTJ pillar, respectively. Kirchhoff's law then gives $\frac{v_b - V_{out}}{0.5R_W} = \frac{V_{SOT} - v_b}{0.5R_W} + \frac{V_{STT}}{R_{MTJ}}$. As V_{out} is initially set to 0 V, we obtain $V_{STT} = \left(v_t - \frac{V_{SOT}}{2}\right) / \left(1 + \frac{R_W}{4R_{MTJ}}\right)$. Assuming $R_W \ll R_{MTJ}$ leads to a simplified expression:

$$V_{STT} \approx v_t - 0.5\,V_{SOT} \quad (2)$$

Owing to the impedance mismatch at the sample edge, a large fraction of each pulse V_0 and V_1 is back-reflected in phase. The resulting voltages at the STT and SOT electrodes are thus the sum of the incoming and reflected pulses, as probed by separate measurements with a tee inserted between the directional coupler and before the device, which gives:

$$v_t = 1.9\,V_1 \text{ and } V_{SOT} = 1.75\,V_0 \quad (3)$$

These measurements agree with the basic theory of impedance-mismatched circuits, for which the applied voltage at the device under test (DUT) is $V_{applied} = \frac{2R_{DUT}}{R_{DUT} + 50\,\Omega} V_{in}$. At the SOT electrode, $R_{DUT} = R_W = 309\,\Omega$, gives $V_{SOT} = 1.72\,V_0$, whereas at the STT electrode, $R_{DUT} = R_{MTJ} = 3.5$–6.5 kΩ, which gives $v_t \approx 1.97\,V_1$. Using equations (2) and (3), the STT bias applied to the MTJ can be expressed as a function of V_0, $V_{STT} \approx 1.9\,V_1 - \frac{1.75}{2} V_0$, or as a function of V_{SOT}, $V_{STT} \approx 1.09(x - 0.46)\,V_{SOT}$, where $x = V_1/V_0$. In agreement with the latter equation, the condition for SOT switching without an STT bias, that is, $V_{STT} = 0$ V, is $x = 0.46$. However, $V_{STT} \neq 0$ V is required to probe R_{MTJ} during the time-resolved measurements. To verify that the effect of the bias on the switching was minor when V_{STT} was small, we compared the after-pulse switching probability P_{sw} when $x = 0.46$ ($V_{STT} = 0$) with $x = 0.63$ ($V_{STT} \approx 50$ V for $\tau_p > 5$ s), which was used for time-resolved detection of the SOT switching. In Extended Data Fig. 2, we show that the critical voltages V_c at different τ_p are identical for the two configurations. This indicates that the effect of V_{STT} on switching is negligible when $x = 0.63$, and hence validates the interpretation of these time-resolved measurements as being representative of SOT switching.

Time-resolved measurement and data normalization. To obtain a normalized time trace, V_{sw}, we compared the signal acquired on the oscilloscope during switching (for example, $V_{P\text{-}AP}$) to a non-switching reference time trace acquired when the magnetization remained in the final state (V_{AP}) or in the initial state (V_P) for the same driving pulse, similar to time-resolved measurements of STT switching in 2-terminal devices[11,13,33]. For the measurement of V_{AP}, we initialized the magnetization in the final state and applied the same pulse and field conditions as used for switching. For the measurement of V_P, we initialized the magnetization in the initial state and reversed the direction of the in-plane field H_x to prevent switching. This is not possible for pure STT switching, as the final state only depends on the pulse polarity. Therefore, for STT, we acquired V_P with an out-of-plane field H_z stronger than the coercive field of the free layer, which forced the magnetization to remain in the initial state. Typical conditions were $|\mu_0 H_z| = 300$ mT for P–AP and $|\mu_0 H_z| = 85$ mT for AP–P switching. The procedure used to obtain V_{sw} for P–AP switching is summarized in Extended Data Fig. 3; the AP–P switching is measured and treated in the same manner. Starting from the measured voltage time traces $V_{P\text{-}AP}$ (blue), V_P (green) and V_{AP} (red), we determined the switching signal ($V_{P\text{-}AP} - V_P$) and the reference signal ($V_{AP} - V_P$) by subtracting the initial state (here V_P) from the other two signals. $V_{sw} = (V_{P\text{-}AP} - V_P)/(V_{AP} - V_P)$ corresponds to the variation of the out-of-plane magnetization from the initial state ($V_{sw} = 0$) to the final state ($V_{sw} = 1$). The origin of the dynamics ($t = 0$) is deduced directly from the measurement as the maximum of the derivative of the measured driving signal. The measurements can be performed only within the pulse duration when ($V_{AP} - V_P$) is non-zero. The situation schematized in Extended Data Fig. 3 corresponds to P–AP switching with $V_{SOT} > 0$, for which $V_{P\text{-}AP}$ and V_{AP} are acquired with $H_x > 0$, and V_P is acquired with $H_x < 0$. Examples of measured V_P, $V_{P\text{-}AP}$, $V_{AP\text{-}P}$ and V_{AP} time traces are shown in Extended Data Fig. 4 for both SOT and STT switching.

All the measurements reported here were performed on the same device at room temperature and are representative of other devices with MTJ diameters that range from 80 to 200 nm. In total, 14 different devices were measured.

Micromagnetic simulations. The current-induced magnetization reversal was modelled by combining micromagnetic simulations with finite element simulations of the current and temperature distribution in a simplified magnetic stack. The current flow and temperature increase due to Joule heating were simulated using COMSOL in an MTJ pillar that consisted of a CoFeB layer (1 nm) sandwiched between the W current line (3.7 nm) and the MgO tunnel barrier (1 nm), with layers on top of MgO treated as a unique element of Cu with a total thickness of 12 nm. The diameter of the MTJ was 80 nm and the W line had a rectangular shape with dimensions 30 × 200 nm². The substrate and the planarization material that surrounded the MTJ pillar was SiO_x. The simulated temperature evolution versus time was used as an input to the object-oriented micromagnetic framework code[47], with an included Dzyaloshinskii–Moriya interaction extension module[48] and a custom-built implementation of the damping-like (DL) and field-like (FL) SOT. In the micromagnetic simulations, the MTJ was further simplified to a single CoFeB free layer. We considered the temperature dependence of the magnetization parameters according to established models: the saturation magnetization varied as[49] $M_S(T) = M_{S0}\left(1 - \frac{T}{T_C}\right)^{\beta}$, where M_{S0} and T_C are the saturation magnetization at $T = 0$ K and the Curie temperature, respectively. Similarly, the magnetic anisotropy and exchange stiffness[50] were scaled as $K(T) = K_0\left(\frac{M_S(T)}{M_{S0}}\right)^p$ and $A_{ex}(T) = A_{ex0}\left(\frac{M_S(T)}{M_{S0}}\right)^q$, where K_0 and A_{ex0} represent the anisotropy energy density and exchange stiffness at 0 K. M_{S0}, K_0 and A_{ex0} were selected to match the room-temperature values of the quantities expected for the studied devices ($M_S = 1.1$ MA m^{-1}, $K = 845$ kJ m^{-3} and $A_{ex} = 15$ pJ m^{-1}), whereas the Curie temperature and critical coefficients were taken from literature values for CoFeB/MgO ($T_C = 750$, $\beta = 1$, $p = 2.5$ and $q = 1.7$) (ref. [49]). We further note that the temperature effects in the simulation are deterministic, that is, we did not consider fluctuations of the thermal bath. The SOT effective fields $\mu_0 H_{DL} = -60$ mT and $\mu_0 H_{FL} = -15$ mT, and the Dzyaloshinskii–Moriya interaction strength $|D| = 0.15$ mJ m^{-2}, were kept constant. We further verified that the observed magnetization dynamics was not specific to the particular choice of these parameters. In the simulation, the CoFeB layer magnetization was initially saturated down and let relax for 0.5 ns after applying H_x. A current pulse with a 0.2 ns rising/falling edge and $|j_{SOT}| = 1.10\ (1.22) \times 10^8$ A cm^{-2} amplitude was applied for 10 (1) ns. After the pulse end, the magnetization was let relax for 4 ns. The simulated time traces (Fig. 4b,c) represent the z component of the magnetization computed in a 4 × 4 × 1 nm³ mesh, averaged over the layer and normalized by M_S.

Data availability

The data that support the plots within this paper and other findings of this study are available from the corresponding author upon reasonable request.

References

46. Thomas, L. et al. Perpendicular spin transfer torque magnetic random access memories with high spin torque efficiency and thermal stability for embedded applications (invited). *J. Appl. Phys.* **115**, 172615 (2014).
47. Donahue, M. J. & Porter, D. G. *OOMMF User's Guide Version 1.0* Interagency Report NISTIR 6376 (National Institute of Standards and Technology, 1999).
48. Rohart, S. & Thiaville, A. Skyrmion confinement in ultrathin film nanostructures in the presence of Dzyaloshinskii–Moriya interaction. *Phys. Rev. B* **88**, 184422 (2013).
49. Lee, K.-M., Choi, J. W., Sok, J. & Min, B.-C. Temperature dependence of the interfacial magnetic anisotropy in W/CoFeB/MgO. *AIP Adv.* **7**, 065107 (2017).
50. Moreno, R. et al. Temperature-dependent exchange stiffness and domain wall width in Co. *Phys. Rev. B* **94**, 104433 (2016).

Acknowledgements

This work was funded by the Swiss National Science Foundation (Grant no. 200020-172775), ETH Zurich (Career Seed Grant SEED-14 16-2) and imec's Industrial Affiliation Program on STT-MRAM devices.

Author contributions

E.G., K.G. and P.G. planned the experiments. S.C., F.Y. and K.G. designed and fabricated the samples. E.G. implemented the time-resolved electrical set-up. E.G. and V.K. performed the measurements. G.S. and V.K. performed the micromagnetic simulations. E.G., V.K, K.G. and P.G. analysed the results. E.G. and P.G. wrote the manuscript. All the authors discussed the data and commented on the manuscript.

Competing interests

The authors declare no competing interests.

Additional information

Extended data is available for this paper at https://doi.org/10.1038/s41565-019-0607-7.

Supplementary information is available for this paper at https://doi.org/10.1038/s41565-019-0607-7.

Correspondence and requests for materials should be addressed to E.G., K.G. or P.G.

Peer review information *Nature Nanotechnology* thanks Christian Back, Andrew Kent and the other, anonymous, reviewer(s) for their contribution to the peer review of this work.

Reprints and permissions information is available at www.nature.com/reprints.

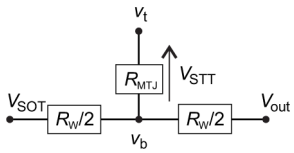

Extended Data Fig. 1 | Equivalent resistance setup of a three-terminal MTJ.

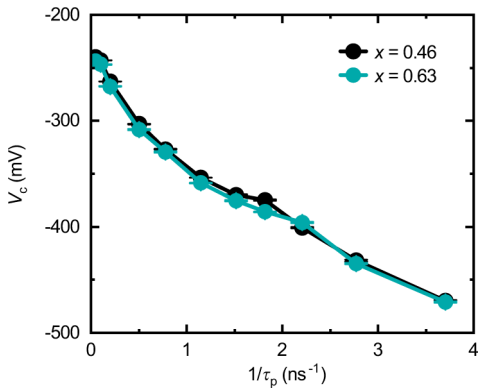

Extended Data Fig. 2 | Comparison of the critical voltage for zero and small STT bias. Critical switching voltage V_c as a function of pulse length τ_p for $x = 0.46$ ($V_{STT} = 0$) and $x = 0.63$ (minimum V_{STT} required to perform time-resolved measurements). The overlap of the data indicates no noticeable effect of the small STT bias on the SOT switching.

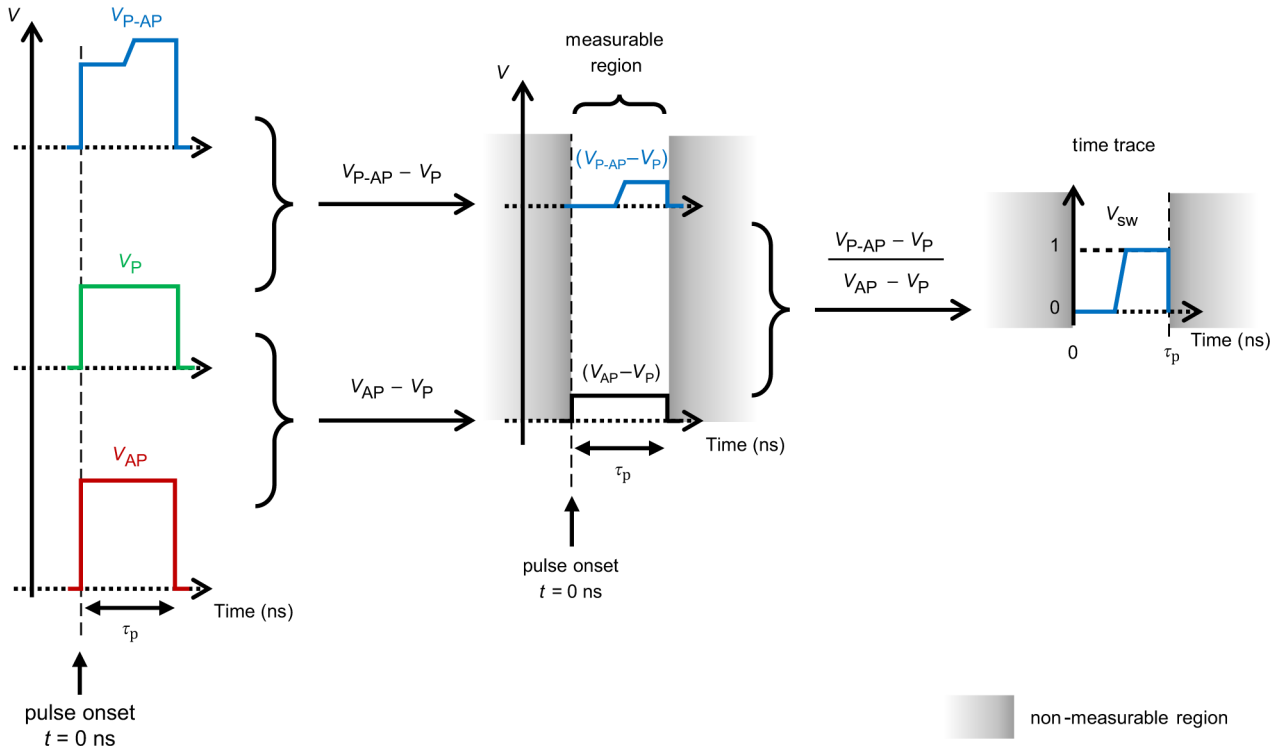

Extended Data Fig. 3 | Schematic of the acquisition and normalization protocol for P-AP switching.

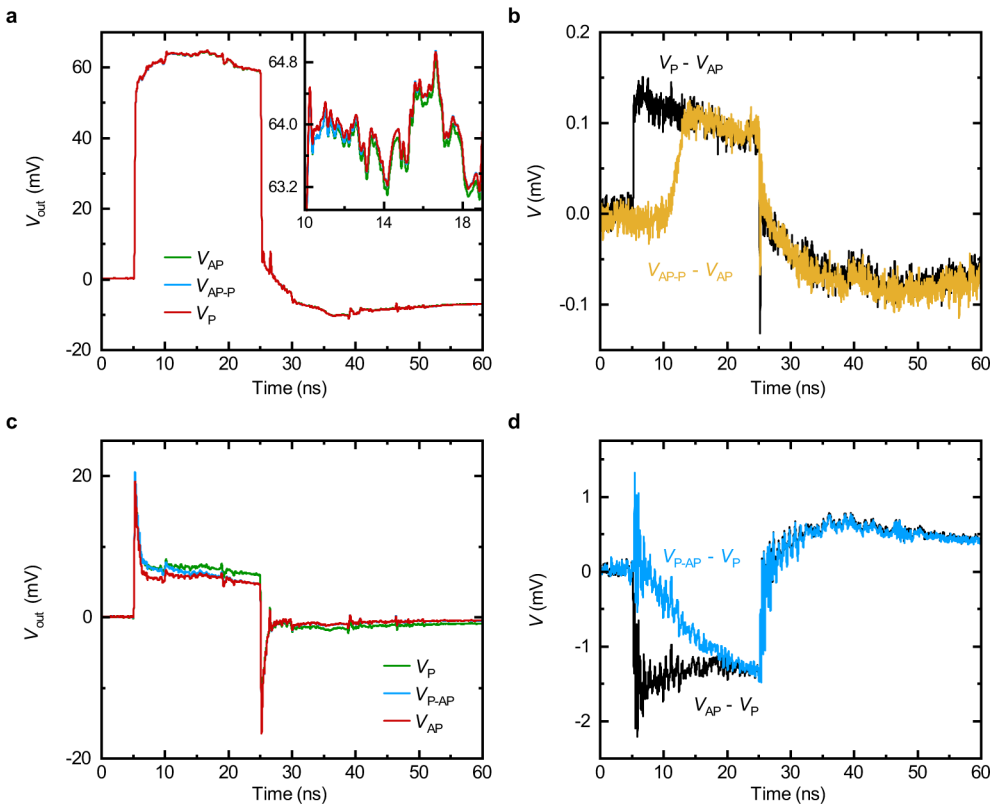

Extended Data Fig. 4 | Examples of V_P, $V_{P\text{-}AP}$, $V_{AP\text{-}P}$ and V_{AP} time traces. a, V_{AP}, $V_{AP\text{-}P}$ and V_P for AP-P SOT switching. **b**, Corresponding switching and reference signals, $V_{AP\text{-}P}$-V_{AP}, and V_P-V_{AP}, respectively. **c**, V_P, V_P-V_{AP}, and V_{AP} for P-AP STT switching. **d**, Corresponding switching and reference signals, $V_{P\text{-}AP}$-V_P and V_{AP}-V_P, respectively. The traces are averaged over 5000 (500) SOT (STT) switching events. These signals are used to obtain the normalized time traces shown in Fig. 2a,b for SOT and STT switching, respectively.

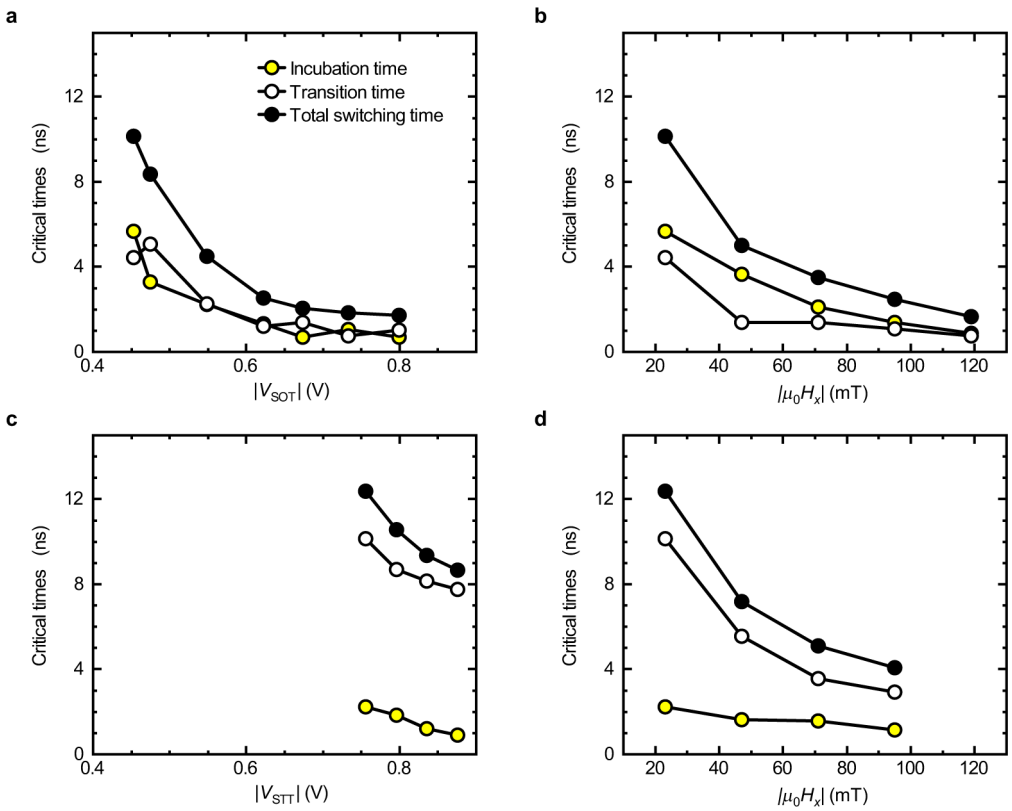

Extended Data Fig. 5 | Average SOT and STT switching times as a function of pulse amplitude and in-plane field. a,**b**, Comparison of the average incubation time and transition time for P-AP SOT switching as a function of pulse amplitude ($V_{SOT} > 0$) at $\mu_0 H_x = -23$ mT (**a**) and in-plane field $\mu_0 H_x$ at $V_{SOT} = +453$ mV (**b**). **c**,**d**, Comparison of the average incubation time and transition time for P-AP STT switching as a function of pulse amplitude ($V_{SST} > 0$) at $\mu_0 H_x = -23$ mT (**c**) and in-plane field $\mu_0 H_x$ at $V_{STT} = +756$ mV (**d**). In **b**,**d**, the pulse amplitude is the minimum allowing 100% switching ($P_{sw} = 1$) at $\mu_0 H_x = -23$ mT.

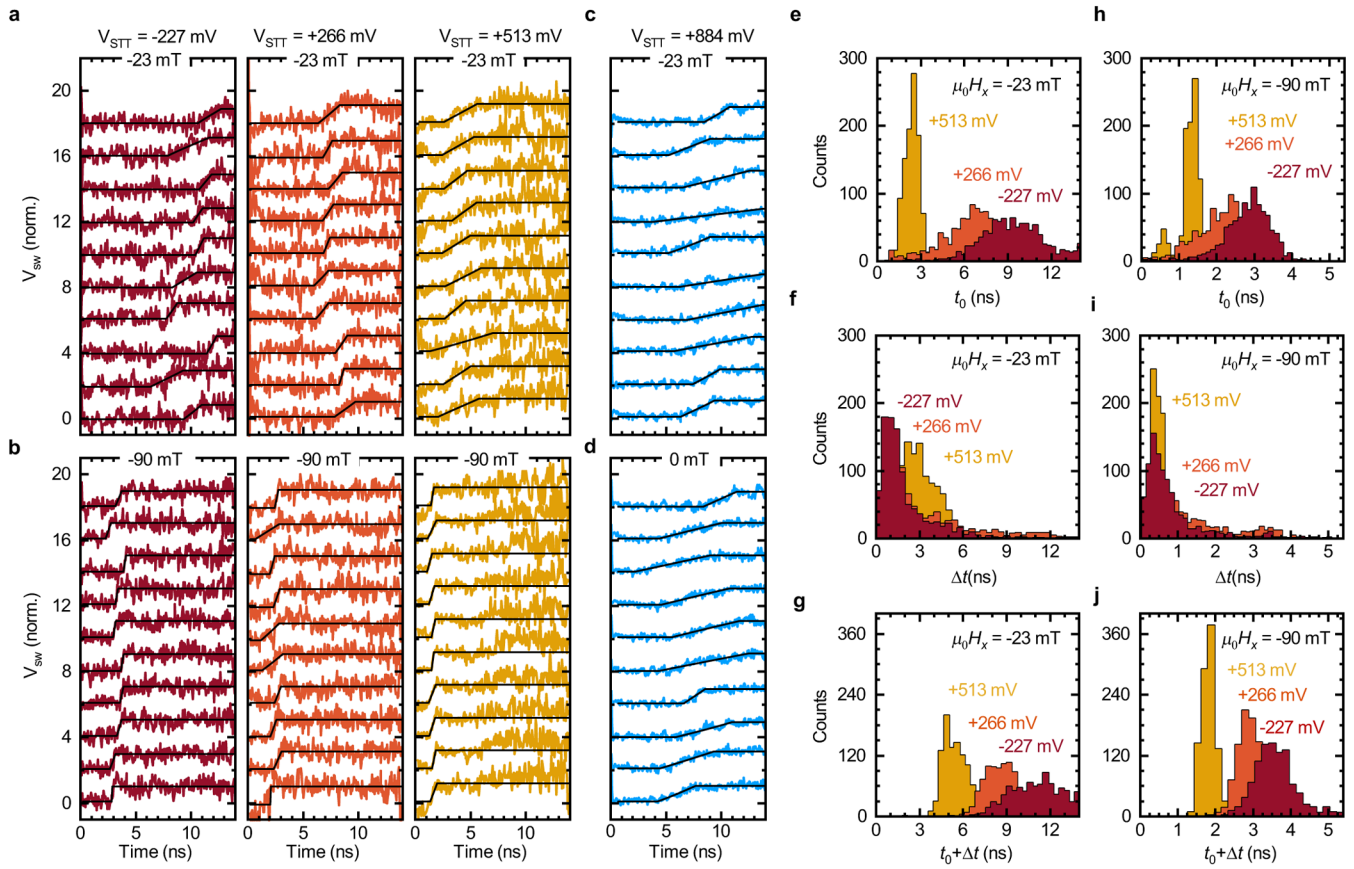

Extended Data Fig. 6 | Single-shot measurements of SOT and STT switching in the AP-P case. a,**b**, Representative time traces recorded during ten individual SOT-induced AP-P switching events induced by 15 ns long pulses with V_{SOT}= +453 mV and increasing STT bias V_{STT}= −227, +266, +513 mV at **a**, $\mu_0 H_x$= +23 mT and **b**, $\mu_0 H_x$= +90 mT. **c**,**d**, Representative time traces recorded during ten individual STT-induced AP-P switching events at V_{STT}= +884 mV and **c**, $\mu_0 H_x$= +23 mT and **d**, $\mu_0 H_x$= 0 mT. The pulse amplitudes are the minimum ones required to achieve 100% switching in any of the shown configurations. The time traces have been vertically offset for clarity. Black solid lines are fits with a linear ramp used for extracting t_0 and Δt. **e**, Statistical distributions of the incubation time t_0, **f**, the transition time Δt and **g**, the total switching time $t_0+\Delta t$ at $\mu_0 H_x$= +23 mT for SOT switching at different STT biases . **h**, Statistical distributions of t_0, **i**, Δt and **j**, $t_0+\Delta t$ at $\mu_0 H_x$= +90 mT. The histograms are obtained from the analysis of 1000 single-shot switching events.

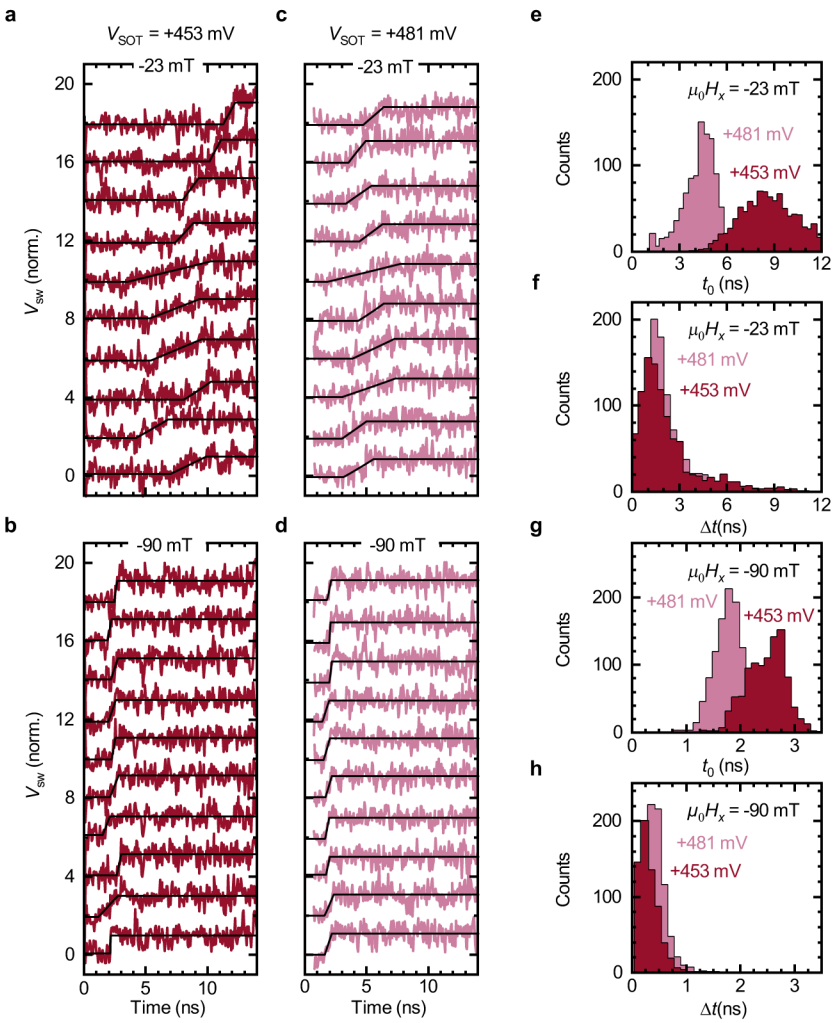

Extended Data Fig. 7 | Single-shot measurements of P-AP switching for different V_{SOT} and H_x. a-d, Representative time traces recorded during ten individual SOT-dominated P-AP switching events induced by 15 ns long pulses with **a**,**b**, V_{SOT}= +453 mV, V_{STT}= −227 mV and **c**,**d**, V_{SOT}= +481 mV, V_{STT}= −242 mV at **a**,**c**, $\mu_0 H_x$= −23 mT and **b**,**d**, $\mu_0 H_x$= −90 mT. The time traces have been offset for clarity. Black solid lines are fits with a linear ramp used for extracting t_0 and Δt. **e-h**, Distributions of **e**, t_0 and **f**, Δt at $\mu_0 H_x$= −23 mT, and **g**, t_0 and **h**, Δt at $\mu_0 H_x$= −90 mT. The histograms are obtained from the analysis of 1000 single-shot switching events.

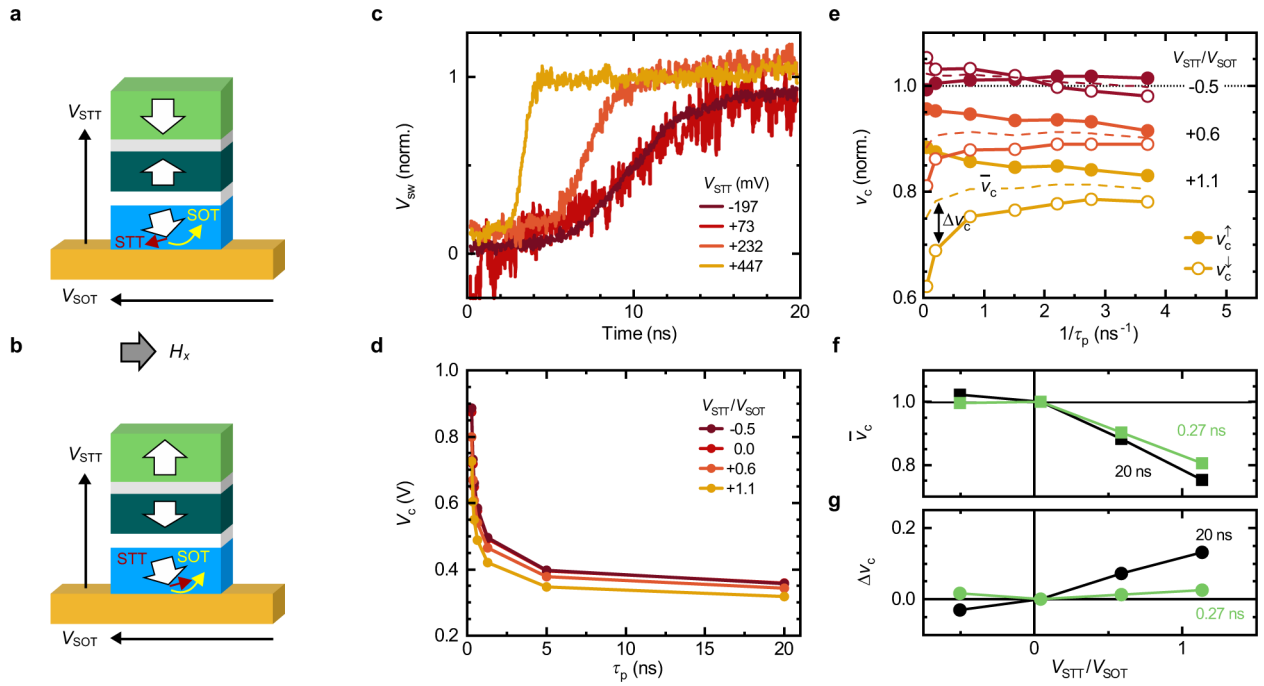

Extended Data Fig. 8 | Combined effect of voltage control of magnetic anisotropy and STT on SOT-induced switching for the free layer initially pointing down. a,**b**, Schematics of the SOT-dominated switching mechanism for the reference layer pointing **a**, up and **b**, down. Black arrows indicate the directions of rf currents, white arrows indicate the magnetization state. The STT (red arrow) given by V_{STT} either **a**, opposes or **b**, assists the SOT switching induced by V_{SOT} (yellow arrow). **c**, Averaged time traces of SOT-induced AP-P switching with V_{STT}= −197, +73, +232, +447 mV for V_{SOT}= +394 mV and τ_p=20 ns. **d**, Evolution of the critical voltage as a function of pulse length for different STT contributions as given by the V_{STT}/V_{SOT} ratio. **e**, Normalized critical voltages $v_c^{\uparrow}$ and $v_c^{\downarrow}$ as a function of inverse pulse length for different V_{STT}/V_{SOT} ratios. The magnetization of the reference layer points either up ($v_c^{\uparrow}$) or down ($v_c^{\downarrow}$), corresponding to the situation depicted in **a**, and **b**, respectively. Evolution of **f**, the average critical voltage $\bar{v}_c$ (VCMA-like contribution) and **g**, voltage asymmetry Δv_c (STT-like contribution) as a function of V_{STT}/V_{SOT} for short and long pulses. All measurements are performed at $\mu_0 H_x$= +90 mT, V_{SOT}>0 and correspond to AP-P (respectively P-AP) switching for the reference layer pointing up (down) and free layer initially pointing down.